Fuel 216 (2018) 407–417

Contents lists available at ScienceDirect

Fuel

journal homepage: www.elsevier.com/locate/fuel

Full Length Article

Effect of carbon-interaction on structure-photoactivity of Cu doped amorphous TiO_2 catalysts for visible-light-oriented oxidative desulphurization of dibenzothiophene

C.N.C. Hitam[a], A.A. Jalil[a,b,*], S. Triwahyono[c], A.F.A. Rahman[a], N.S. Hassan[a], N.F. Khusnun[a], S.F. Jamian[c], C.R. Mamat[c], W. Nabgan[a,d], A. Ahmad[a,b]

[a] Department of Chemical Engineering, Faculty of Chemical and Energy Engineering, Universiti Teknologi Malaysia, 81310 UTM Johor Bahru, Johor, Malaysia
[b] Centre of Hydrogen Energy, Institute of Future Energy, Universiti Teknologi Malaysia, 81310 UTM Johor Bahru, Johor, Malaysia
[c] Department of Chemistry, Faculty of Science, Universiti Teknologi Malaysia, 81310 UTM Johor Bahru, Johor, Malaysia
[d] Catalysis Research Division, Research Institute of Petroleum Industry (RIPI), Tehran, Iran

GRAPHICAL ABSTRACT

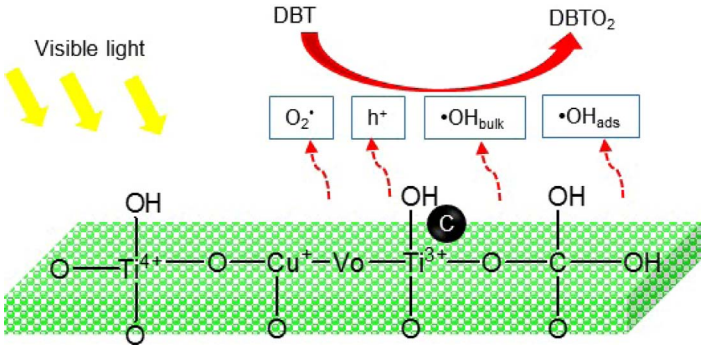

ARTICLE INFO

Keywords:
Ti-precursor
C-interaction
Amorphous TiO_2
Visible-light-oriented
Oxidative desulphurization

ABSTRACT

Amorphous TiO_2 (AT) was successfully prepared via the sol-gel technique, using different titanium sources followed by incorporation of copper via the electrochemical method to give CuO/TiO_2 (CAT) catalysts. The catalysts were characterized via XRD, N_2 physisorption, FTIR, TEM, EDX, XPS, ESR and UV–Vis DRS. The results verified that the use of different titanium precursors have profound effect on the physicochemical properties of the AT catalysts. Further one-pot self-doping carbon from titanium precursor during the addition of copper could greatly enhanced the photocatalytic activity of CAT on the oxidative desulphurization of dibenzothiophene (DBT). 15 CAT_{TBOT} exhibited the best performance mainly due to the narrowest band gap and higher numbers of O–Ti–C and Ti–O–C bonds, as well as appropriate amount of Ti^{3+} surface defects (TSD). These abovementioned properties offered good mobility of electron-hole pairs and/or trap the electrons for enhancement of photo-activity under irradiation of visible light. Kinetic studies showed that the photocatalytic oxidative desulphurization of DBT followed the pseudo-first order Langmuir-Hinshelwood model, where the adsorption was the

Abbreviations: SO_x, sulphur oxide; TBOT, titanium tetrabutoxide; TTIP, titanium tetraisopropoxide; TEAP, tetraethylammonium perchlorate; V_o, oxygen vacancies; TSD, Ti^{3+} surface defects; PP, potassium peroxodisulphate; TEOA, triethanolamine; SHC, sodium hydrogen carbonate; IP, isopropanol; VB, valence band; CB, conduction band

* Corresponding author at: Department of Chemical Engineering, Faculty of Chemical and Energy Engineering, Universiti Teknologi Malaysia, 81310 UTM Johor Bahru, Johor, Malaysia.
E-mail address: aishahaj@utm.my (A.A. Jalil).

https://doi.org/10.1016/j.fuel.2017.12.035
Received 13 August 2017; Received in revised form 17 November 2017; Accepted 7 December 2017
Available online 14 December 2017

controlling step. It is believed that these results could contribute to the synthesis of various supported catalysts for numerous applications specifically in removal of sulphur containing compounds in fuel oils.

1. Introduction

The release of SO_x which mainly formed via the burning of sulphur-containing compounds in fuel oils is one of the most serious worldwide environmental concerns [1]. In order to minimize its harmful influence on human health and the environment, the reduction of sulphur content in fuel is urgently required [2–4]. Photocatalytic degradation process using heterogeneous catalysts is fascinating and prominent for environmental protection as an environmental friendly, low cost, and sustainable technology [5]. Among photocatalytic materials, TiO_2 is widely used for degradation of dyes and organic pollutants, as well as for the removal of inorganic materials due to its excellent photoactivity [6]. However, TiO_2 only responds to ultraviolet radiation due to its large band gap (3.2 eV) and fast electron-hole recombination rate, which causes difficulties with respect to its practical application [7]. As a result, great effort has been expended toward the improvement of new visible-light-responsive photocatalysts.

Among the various types of TiO_2 catalysts, amorphous TiO_2 nanoparticles have experienced intensive advances, and a growing number of studies have started to challenge the belief that the amorphous TiO_2 is not photoactive [8]. As compared to crystalline TiO_2, amorphous TiO_2 is easily prepared, owing to its lower demand of substrate [9]. It also does not require heat treatment processes, and may allow the use of a much wider range of dopants. Amorphous TiO_2 has been used for various photocatalytic reactions such as hydrogen evolution from water, decolourization of methylene blue and disinfection of algae blooms, as well as oxidative desulphurization of dibenzothiophene [10–12].

Previous study showed that the use of different titanium precursor to synthesize amorphous TiO_2 has contributed to dissimilar pore size distribution and surface area [13]. The presence of long chain carbon might reduce hydrolysis and condensation rate and restrict the particle nucleation, thus yields aggregated bigger particles with small surface area and high pore volume. During hydrolysis, Ti-alkoxide react with water to form $Ti(OH)_4$ and alcohol, which subsequently polymerized to a three-dimensional oxide network [14]. The alcohol group that formed after hydrolysis process are determined by the carbon chain of alkoxide and subsequent drying or calcination might remove these species.

Recently, it has been reported that band gap modification via non-metal doping such as C, N, S, F and B can produce highly active TiO_2 photocatalysts [15]. Non-metal doping is a promising way to enhance the photoabsorption properties of TiO_2 by lowering the band gap and shift the absorption edge to the visible light region [16]. It is believed that bulk doping or matrix substitution can introduce interior electron states within the band gap and thus shift the response and harvest visible light for applications in photocatalysis [17]. In addition, the combination of TiO_2 with other semiconductors with narrow band gaps is also an efficient pathway to extend the visible light response of TiO_2-based catalysts. For coupling with TiO_2, nanosized CuO is an ideal candidate due to its proper band edge, low cost, low toxicity, and abundant supply [18].

In recent years, numerous nanosized particles of ZnO, α-FeOOH and NiO supported on mesostructured silica nanoparticles (MSN), Ag supported on mesoporous TiO_2 nanoparticles (MTN) and also CuO supported onto carbon nanotubes (CNT) were successfully prepared via a facile electrochemical technique [19–22]. Their excellent performances in the photocatalytic degradation of dyes and organic pollutants, along with CO_2 reforming of CH_4, would encourage additional modification. In previous work, the electrochemical method provided a stronger interaction between the dopant and support, and consequently lessened the agglomeration of dopant, thus forming uniform and smaller dopant particles [23]. Therefore, herein we report new findings on (i) self-doped C via the electrochemical method for synthesis of CuO loaded onto AT catalysts, and (ii) their enhanced performance towards photocatalytic oxidative desulphurization of DBT under visible light irradiation. The physicochemical properties of the catalysts were well characterized by X-ray diffraction (XRD), N_2 physisorption, Transmission electron microscopy (TEM), energy dispersive X-ray (EDX), Fourier transform infrared (FTIR), X-ray photoelectron spectroscopy (XPS), electron spin resonance (ESR), and ultraviolet–visible diffuse reflectance spectroscopy (UV–Vis DRS). The proposed structure of the catalyst, kinetic studies, and the proposed mechanism of photo-oxidative desulphurization are also discussed. We believe that this study could contribute to future design approaches for numerous organic pollutants and other reactions.

2. Experimental

2.1. Materials

Titanium tetrabutoxide (TBOT) was purchased from Merck Sdn. Bhd., Malaysia. Other chemicals used were similar with those used and prepared by earlier reported studies [24,25].

2.2. Synthesis of catalyst

The amorphous TiO_2 was synthesized by sol-gel technique using TTIP or TBOT as titanium precursor and denoted as AT_{TTIP} and AT_{TBOT}, respectively [25]. The CuO/TiO_2 amorphous were synthesized via electrolysis method using AT_{TBOT} as support, based on previous reported study with some modification [25–27].

2.3. Characterization of the catalyst

The structural properties of the catalysts were determined with X-ray diffraction (XRD) recorded on powder diffractometer (Bruker Advance D8, 40 kV, 40 mA) using a Cu Kα radiation source. Beckman Coulter SA 3100 surface area analyzer was used in N_2 physisorption analysis to study the textural properties which is conducted at 77 K. Prior to measurement, the samples were degassed at 373 K for 1 h. The Brunnauer-Emmett-Teller (BET) method was used to calculate surface area from the N_2 adsorption isotherms. FTIR was performed by the KBr method using PerkinElmer Spectrum GX FTIR spectrometer in the range of 400–4000 cm^{-1}. Transmission electron microscopy (TEM) was used to examine the morphological properties using JEOL JEM-2100F while energy dispersive X-ray (EDX) was carried out to identify the chemical composition of the catalysts. The X-ray photoelectron spectroscopy (XPS) was conducted on a Shimadzu Axis Ultra DLD spectrometer, using Al X-ray source over binding energies of 0–800 eV to determine the chemical oxidation of the catalyst. The electron spinning resonance (ESR) analysis was performed using JEOL JESFA100 ESR spectrometer at room temperature. UV–Vis diffuse reflectance spectra (UV–Vis DRS) using a PIKE Technologies DiffusIR in the range of 300 to 800 nm was conducted at room temperature to examine the band gap of the catalysts.

2.4. Photocatalytic oxidative desulphurization reaction

The photocatalytic oxidative desulphurization of dibenzothiophene (DBT) were carried out in a batch reactor as reported in our previous

study [25].

3. Results and discussion

3.1. Characterization of the catalyst

Two types of amorphous TiO_2 catalysts were used for photocatalytic oxidative desulphurization of dibenzothiophene (DBT), which were prepared from two different titanium sources; titanium tetraisopropoxide (TTIP) and titanium tetrabutoxide (TBOT), denoted as AT_{TTIP} and AT_{TBOT}, respectively. The pore width distribution of both catalysts were calculated by Barrett-Joyner-Halenda (BJH) method as shown in Fig. 1. The AT_{TBOT} consists of mainly larger bimodal pore structure, in the range of 20–100 nm, as compared to AT_{TTIP} with bimodal pore structure in the range of 3–50 nm. The existence of longer carbon chains in TBOT might lead to a lower hydrolysis and condensation rate, which limits particle nucleation and produces aggregated larger particles with lower surface area and higher pore volume (Table 1) [28,29]. The higher pore volume of AT_{TBOT} could provide more sites for DBT molecules to be adsorbed, which subsequently enhance photooxidation [30]. Although it was reported that the larger pore size could only weaken the attraction toward adsorbate via dispersive forces, its important role in enhancing the adsorption capacity of the desired reaction could not be ruled out [31]. Similar phenomenon was reported previously on the adsorption of DBT by activated carbon, where the adsorption capacity considerably influenced by the pore size distribution rather than the surface area [32].

3.1.1. Structural studies

Due to the higher performance of the AT_{TBOT}, it was chosen as a model catalyst and supported with the lower band gap of CuO via electrochemical method and denoted as CAT_{TBOT} [25]. Two different loading of CuO, 5 and 15 wt% were investigated, and Fig. S1 shows the XRD pattern of AT_{TBOT} and both CAT_{TBOT}. As can be seen, only a broad peak between 2θ = 20–30° is found in AT_{TBOT}, with no distinct peak of TiO_2, signifying the presence of an amorphous structure [33]. A similar characteristic peaks to AT_{TBOT} were observed for CAT_{TBOT}, proving the preservation of the amorphous phase of TiO_2 even after the addition of higher Cu loading (Fig. S1/c).

3.1.2. Study of textural properties

Fig. 2A shows the N_2 physisorption isotherms of both CAT_{TBOT}, while their corresponding textural properties are listed in Table 1. It was seen that the AT_{TBOT} demonstrated a common adsorption profile for a mesoporous material and classification of slit shaped pores as shown by a type IV isotherm curve and H3 hysteresis loop (Fig. 2A/a), accordingly [21,34]. Two up-steps at P/P_o = 0.3 and 0.9 demonstrated the capillary condensation of N_2 in the intraparticle and interparticle mesopores, respectively [35]. The CuO loading seems to reduce the number of interparticle pores drastically, and it was clearly observed from the pore size distribution presented in Fig. 2B (inset figure) that the bimodal pore structure of AT_{TBOT} was significantly decreased. Increasing the CuO loading further blocked the mesopores and decreased the pore diameter of the catalysts, which consequently reduced the surface area and pore volume (Table 1).

3.1.3. Morphological studies

TEM analysis was conducted to study the morphological properties of the AT_{TTIP}, AT_{TBOT} and 15 CAT_{TBOT} catalysts and the images are displayed in Fig. 3. As can be seen in Fig. 3A-B, both AT_{TTIP} and AT_{TBOT} consist of aggregated ultrafine nanoparticles, in which the latter shows larger particles in the range of 10–30 nm, resulting from a lower hydrolysis and condensation rate due to the presence of longer carbon chains in TBOT [28]. The HRTEM of the AT_{TBOT} (Fig. 3C) shows no evidence of crystal grains formation and the absence of crystal planes, proving the amorphous nature of the catalyst, which is in agreement with the XRD result [8]. Meanwhile, the presence of CuO nanoparticles on the 15 CAT_{TBOT} was confirmed by its interplanar distance of 0.2720 nm as shown in inset figure of Fig. 3D. To further identify the elemental compositions and dispersion state of the dopants on 15 CAT_{TBOT}, EDX analysis equipped with elemental mapping was performed and the results were shown in Figs. S2 and 3E–G, respectively. The EDX spectrum (Fig. S2) further confirmed the presence of Cu, C and N in the AT_{TBOT} support. In addition, the dispersion of all dopants was noticeably observed by EDX mapping as shown in the Fig. 3E–G.

3.1.4. Vibrational spectroscopy

The FTIR analysis was then performed between the region of 1600 and 400 cm^{-1} and the spectra are presented in Fig. 4A. Comparing with AT_{TTIP} (Fig. 4A/a), the AT_{TBOT} (Fig. 4A/b) displays an obvious peak at 1460 cm^{-1}, attributing to a CH_2 scissoring, which is supposed to originate from the diffusion of carbon chain of butoxide after hydrolysis [19]. This may give significant effect on the higher performance of the AT_{TBOT} rather than AT_{TTIP}. Meanwhile, the aforementioned peak for both 5 CAT_{TBOT} (Fig. 4A/c) and 15 CAT_{TBOT} (Fig. 4A/d) catalysts became stronger after electrolysis process, and strong triplet bands corresponding to C–N stretching appeared at 1083–1141 cm^{-1}, signifying the probable contribution of the supporting electrolyte TEAP on the AT_{TBOT} support [25,36]. A small peak was also detected at 1005 cm^{-1} after the electrolysis, which could be attributed to C–O and/or Ti–O–C bond that might also originate from the TEAP or trace butanol in the AT_{TBOT} [37]. In order to further confirm the presence of the abovementioned non-metal species, 15 CAT_{TBOT} was calcined at 873 K and denoted as 15 $CAT_{TBOTcal}$ (Fig. 4A/e). It can be seen that the related species were totally removed after calcination process, confirming the fact of the postulation above. Next, the broad band at 800–400 cm^{-1} was investigated via Gaussian curve-fitting. As presented in Fig. S3, four strong bands were detected at 735–475 cm^{-1}, which were attributed to Ti–O–Ti vibration modes [38]. For better view, the intensities of the abovementioned bands are summarized in Fig. 4B. It can be seen that the Ti–O–Ti vibration mode decreased with the increasing CuO loading to produce the Ti–O–C bonds, elucidating the involvement of carbon sourced from TEAP in the interaction with the AT_{TBOT} support [39].

For further investigation on the hydroxyl groups of the catalysts, the catalysts were evacuated for 1 h at 623 K to eliminate the physisorbed water and the spectra are presented in Fig. 4C. Three leading bands

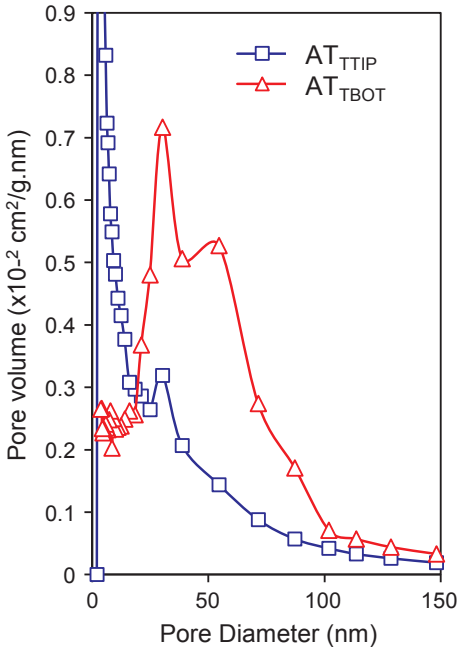

Fig. 1. Pore distribution of AT_{TTIP} and AT_{TBOT}.

Table 1
Textural properties of the catalysts.

Catalyst	Surface area ($m^2 g^{-1}$)	Total pore volume ($\times 10^{-1} cm^3 g^{-1}$)	Band gap, E_g (eV)[a]
AT_{TTIP}	402	4.51	3.16
AT_{TBOT}	355	5.14	3.26
5 CAT_{TBOT}	198	2.80	2.95
15 CAT_{TBOT}	181	2.38	2.56
15 $CAT_{TBOTcal}$	–	–	2.70

[a] Band gap derived from 1240/λ equation.

were perceived at 3750, 3735 and 3712 cm^{-1}, which were attributed to germinal, terminal and bridged hydroxyl groups of the AT_{TBOT} [18,40,41]. The first two bands seems to reduce by the increasing CuO loading, while the latter band slightly shifted to 3715 cm^{-1}, verifying the perturbation of titania framework by the presence of carbon dopant [5]. Moreover, the electrolyzed Cu ions are also supposed to interact with the germinal hydroxyl groups of AT_{TBOT} to form Ti–O–Cu(I) bonds, as reported in our previous study [25]. Thus, it could be dictated that besides Cu- and N-, the C- also interacted with the AT_{TBOT} support.

3.1.5. Chemical oxidation state determination

In order to clarify the exact structure of the catalysts, 5 CAT_{TBOT} and 15 CAT_{TBOT} were then subjected to XPS analysis, and the results were compared with the parent AT_{TBOT}. The XPS spectra of Ti 2p in the region of 470–450 eV was displayed in Fig. 5A. An obvious peak set corresponding to the Ti^{4+} state (Ti $2p_{1/2}$ and $2p_{3/2}$) was detected for AT_{TBOT} (Fig. 5A/a). The introduction of dopants noticeably decreased the intensity and split to two peak sets of Ti^{4+} and Ti^{3+} states (Fig. 5A/b and A/c). It was observed that after electrolysis, the Ti^{4+} ions were reduced to Ti^{3+} state to allow the generation of oxygen vacancies (V_o) [18]. However, the increasing in electrolysis time seems to decrease the amount of Ti^{3+}, indicating the loss of V_o, possibly due to the incorporation of C atom into V_o to form O–Ti–C bond. Fig. 5B presents the deconvolution results of C 1 s in the region of 290–280 eV. The peak at 283.5 eV corresponded to C–C bond which might originate from butanol residues and ethyl groups derived from TEAP [42]. The other peak at around 285.7 eV is attributed to C–H bonds, while the O–Ti–C, Ti–O–C and C–N stretching peaks for CAT_{TBOT} were detected at 282.3, 286.6 and 287.4 eV, respectively [43,44]. The formation of carbon atoms in the interstitial positions of the TiO_2 lattice can occur by replacing titanium atoms in the form of Ti–O–C, while O–Ti–C bonds result from the substitution of V_o by a carbon atom [45]. From overall spectra, it can be summarized that the longer the electrolysis time, the higher amount of O–Ti–C or/and Ti–O–C bonds was formed, which contribute to the decreasing in Ti^{3+} species. These results verified the possible interaction of C that is originated from butanol residues and/or TEAP with AT_{TBOT}, which is in line with the FTIR data.

Next, the ESR analysis were performed to study the electronic structure of the catalysts and the results are shown in Fig. 6A. A strong signal was observed for CAT_{TBOT} at g = 1.94, corresponding to the high amount of Ti^{3+} surface defects (TSD), which is in accordance with the XPS data (Fig. 5A). The decrease in TSD signal with increasing electrolysis time also verified the reduction of V_o due to the formation of O–Ti–C bonds (Fig. 6B) [46]. This was in parallel with the consumption of TEAP, as confirmed by the FTIR and further supported by the XPS analysis.

The band gap energy (E_g) of the catalysts were calculated by equation $E_g = 1240/\lambda$, based on the UV–vis DRS spectra as shown in Fig. 7A. The observed E_g were then tabulated in Table 1. AT_{TBOT} with a band gap of 3.26 eV, shows a red shift in absorption edge by the incorporation of dopants, demonstrating a significant improvement of the catalysts toward visible light absorption. In order to further confirm that the narrow band gap of the catalyst was also influenced by C, not by the Cu dopant only, the band gap of 15 CAT_{TBOT} was compared with 15 $CAT_{TBOTcal}$. It can be noted that the band gap of 15 $CAT_{TBOTcal}$ was higher, further supporting the contribution of non-metal elements in lowering the band gap of catalysts [47]. The presence of O–Ti–N bond that creating N-induced mid-gap was reported in our previous study [25]. However, in this study, the O–Ti–C bond also produces a new impurity level between the conduction and valence band of TiO_2 [17]. The existence of those impurity level was then clarified by Tauc's plot of $(\alpha E)^{0.5}$ versus E (eV) for 15 CAT_{TBOT} as shown in Fig. 7B. It can be seen that, there are two band gap energies detected in the catalyst, in which the lower value (1.60 eV) might attributed to E_g between valence band and interbands, and 2.56 eV represents the E_g between the valence and conduction band [42]. It has been previously reported that impurity level could provide much easier electron excitation under visible light irradiation, thus more photogenerated electron-hole pairs might being produced for a better photoactivity [48].

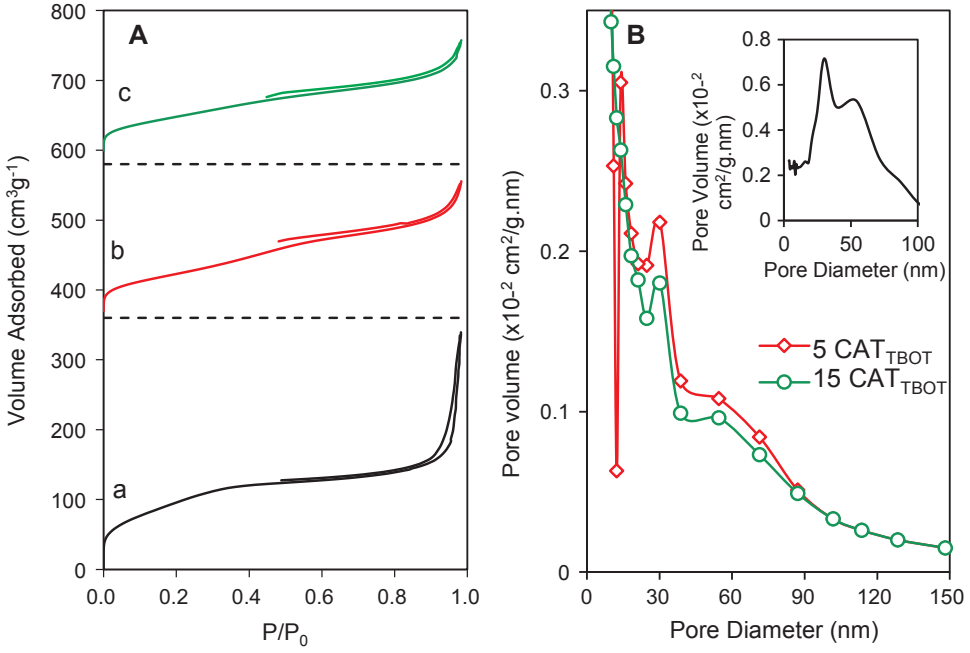

Fig. 2. (A) Nitrogen adsorption-desorption isotherm of a) AT_{TBOT}, b) 5 CAT_{TBOT} and c) 15 CAT_{TBOT} and (B) Pore distribution of catalysts, and (inset figure) AT_{TBOT}.

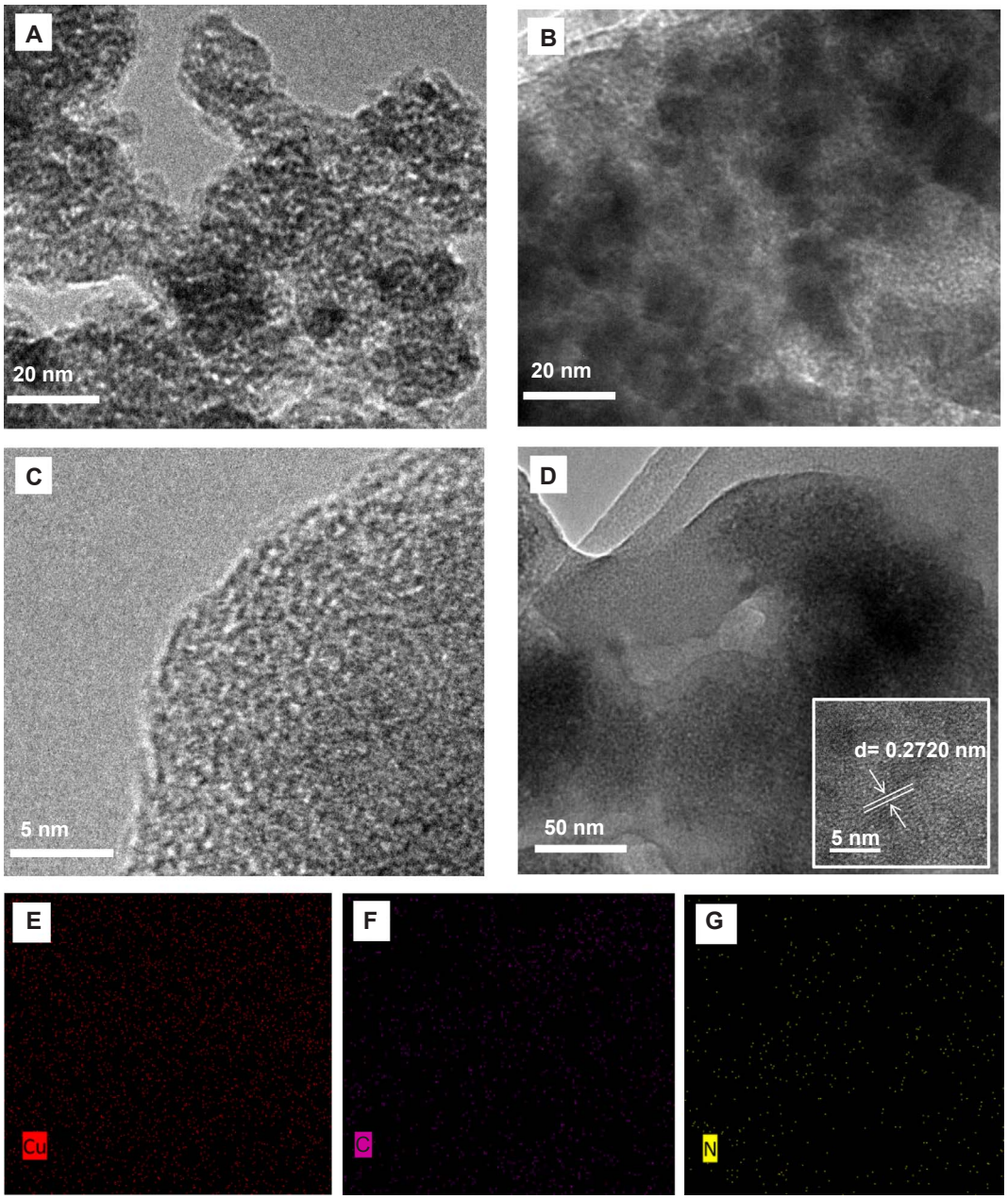

Fig. 3. TEM images of (A) AT_{TTIP}, (B and C) AT_{TBOT}, (D) 15 CAT_{TBOT} and (inset figure) HRTEM images of 15 CAT_{TBOT}, and EDX elemental mapping of (E) Cu, (F) C and (G) N of 15 CAT_{TBOT}.

3.2. Proposed structure of the catalysts

A probable structure of the AT_{TBOT} and CAT_{TBOT} are then illustrated in Fig. 8 according to the above characterization results. In the presence of water, alkoxides (TBOT) were hydrolyzed, forming butanol and Ti $(OH)_4$, which then polymerized to form a three-dimensional AT_{TBOT} oxide network [49,28]. Electrolysis of the AT_{TBOT} in the presence of the weak base TEAP then led to the introduction of C and Cu to form Ti–O–C, O–Ti–C and Ti–O–Cu(I) bonds into the AT_{TBOT} network, as verified by the FTIR and XPS data [37,21,50]. Noticeably, oven dried AT_{TBOT} at 383 K allowed self-doped C into the AT_{TBOT} network, which originated from butanol residue in the system [51]. Based on the FTIR and XPS data, the O–Ti–C and Ti–O–C bonds seemed to dominate prior to the Ti–O–Cu(I) bond, and these occurrences also resulted in the decline of TSD and V_o, as confirmed by the ESR analysis. During electrolysis, Cu is considered as the last element that entered the TiO_2 network after C. The C might be originated from trace of butanol and TEAP supporting electrolyte. It is reported previously that the structure of support can be affected by sequence of dopants introduction, in which C might dispersed homogenously on AT_{TBOT} support and hindered a possible inclusion of Cu [5]. Furthermore, due to the smaller atomic radii of C (70 pm) as compared to Cu (128 pm), as well as its higher electronegativity, led to easy formation of Ti–O–C than Ti–O–Cu (I) bond, as a consequence of removal of Ti^{4+} during electrolysis.

3.3. Photocatalytic oxidative desulphurization performance and proposed mechanism

As shown in Fig. 9A, the AT_{TBOT} performed better in both extraction and photooxidation than the AT_{TTIP} with the rates of 7.32×10^{-3} and 1.29×10^{-3} mM min^{-1}, respectively. These could be generally explained by the pore width distribution displayed in Fig. 1, in which the higher pore volume of AT_{TBOT} provided more adsorption sites for DBT molecules, thus enhanced photooxidation. Overall, 15 CAT_{TBOT}

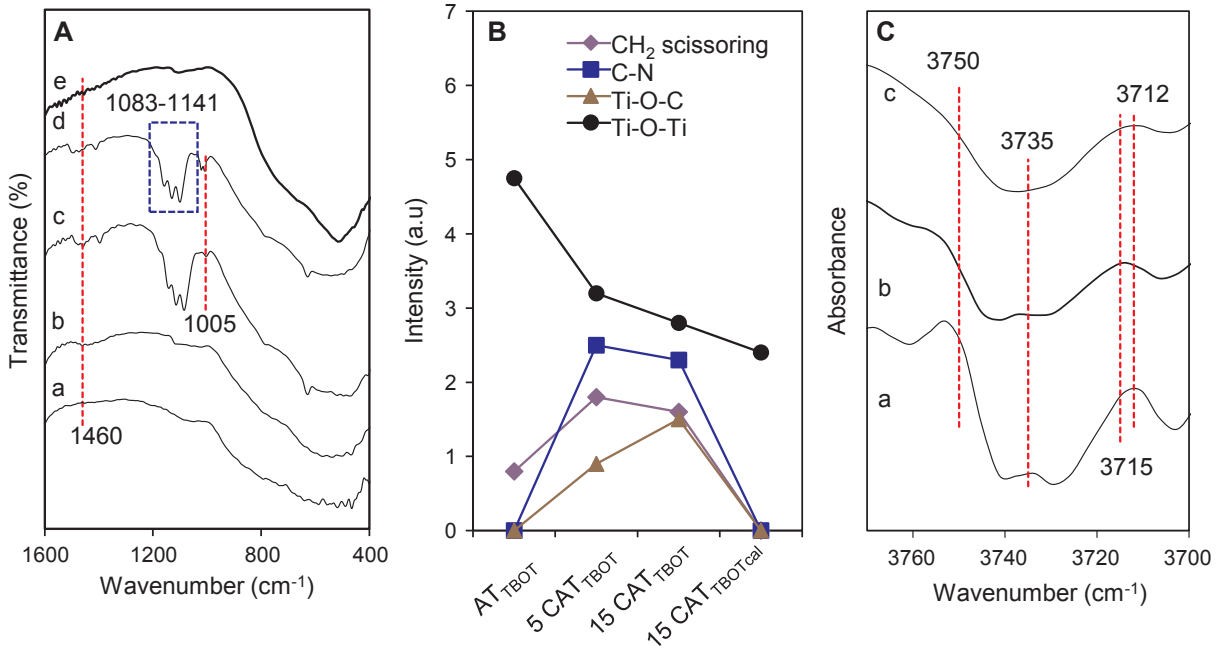

Fig. 4. (A) FTIR spectra of a) AT_{TBOT}, b) 5 CAT_{TBOT}, c) 15 CAT_{TBOT} and d) 15 $CAT_{TBOTcal}$, (B) Intensity of the peaks in the 1600–400 cm^{-1} region and (C) In evacuated system for region 3770–3700 cm^{-1} of a) AT_{TBOT}, b) 5 CAT_{TBOT} and c) 15 CAT_{TBOT}.

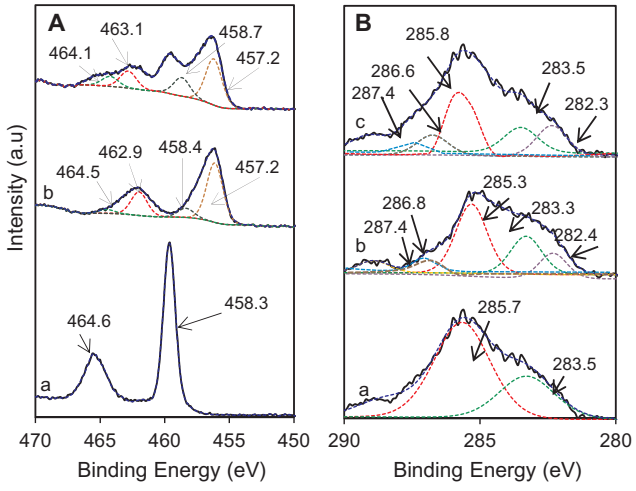

Fig. 5. XPS spectra of (A) Ti 2p a) AT_{TBOT}, b) 5 CAT_{TBOT} and c) 15 CAT_{TBOT} and (B) C 1s a) AT_{TBOT}, b) 5 CAT_{TBOT} and c) 15 CAT_{TBOT}.

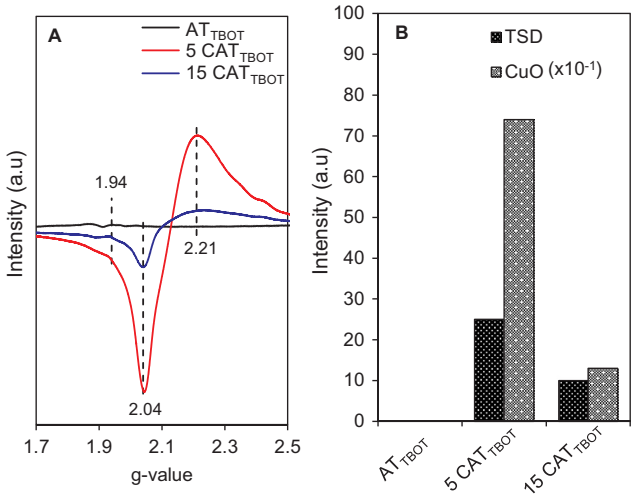

Fig. 6. (A) ESR signals of the catalysts, (B) Intensity of TSD and CuO signals.

demonstrated the best performance compared to other catalysts with the extraction and photooxidation rate of 8.14×10^{-3} and 2.13×10^{-3} mM min^{-1}, respectively. The adsorption capacity of 15 CAT_{TBOT} towards DBT molecules might be lower than other catalysts due to its lowest surface area and pore volume (Table 1). However, the higher rate shown by 15 CAT_{TBOT} may be due to the existence of the narrowest band gap, good interactions between C with AT_{TBOT} support, and physical properties, which enhanced its photoactivity under visible light. Its larger number of O–Ti–C and Ti–O–C bonds, as well as an appropriate surface area and pore volume, increased the number of active sites and offered good surface contact with light to transport and/or trap electrons for enhancement of photoactivity. From the figure, it also could be clearly observed that 20 CAT_{TBOT} showed a lower extraction and photooxidation rates than 15 CAT_{TBOT}. This is most probably due to the agglomeration of Cu when excess of Cu was loaded onto AT_{TBOT}, which further blocked the light penetration, thus decreased the activity [52].

Fig. 9B shows the linear plot of ln (C_0/C_t) vs. irradiation time of

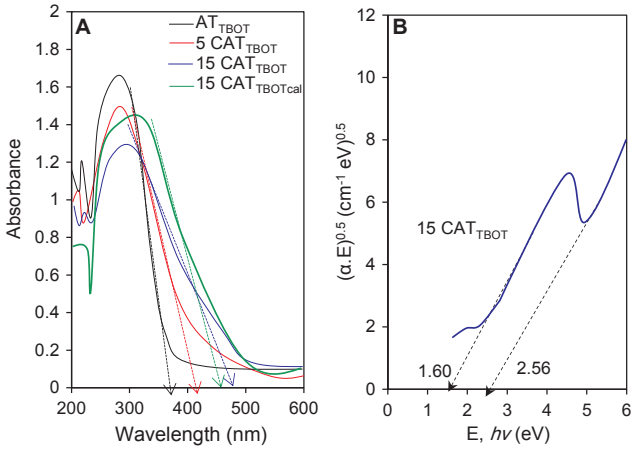

Fig. 7. Tauc plot of the catalysts.

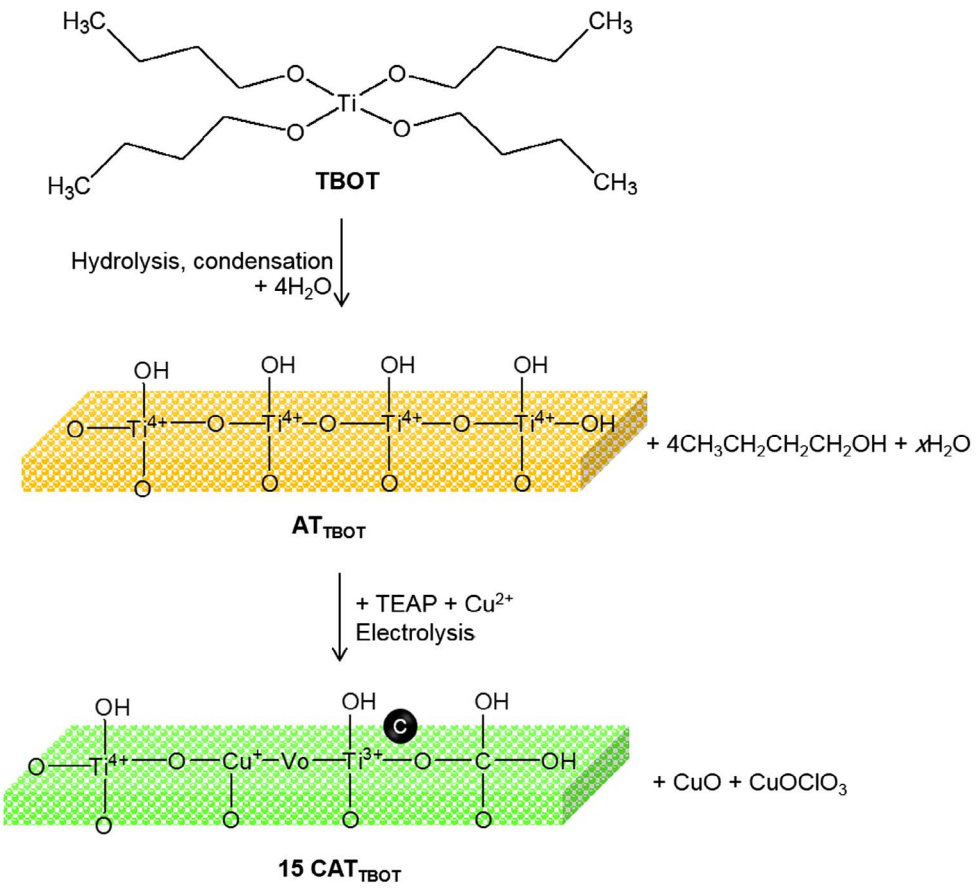

Fig. 8. Proposed structure of 15 CAT_{TBOT} catalyst.

photooxidation of DBT for initial concentrations in the range of 100 to 300 mg L^{-1} using 0.8 g L^{-1} of 15 CAT_{TBOT}. The obtained straight line confirmed that the reaction followed the pseudo-first order kinetic of the Langmuir-Hinshelwood model [53]. A noteworthy effect of 15 CAT_{TBOT} on the photooxidation of DBT was shown by the k_{app} values listed in Table 2. It can be seen that the k_{app} value decreased inversely proportional with initial concentration, signifying that the DBT was saturated on the catalyst surface thus reduced the photooxidation effectiveness, and the system was less favourable at high concentrations [54]. The values of k_r (reaction rate constant) and k_{LH} (adsorption coefficient of the reactant) were 0.296 mg L^{-1} min^{-1} and 0.036 L mg^{-1}, respectively (figure not shown), demonstrating that adsorption of DBT was the controlling step [55].

In order to examine the mechanism of photocatalytic oxidative

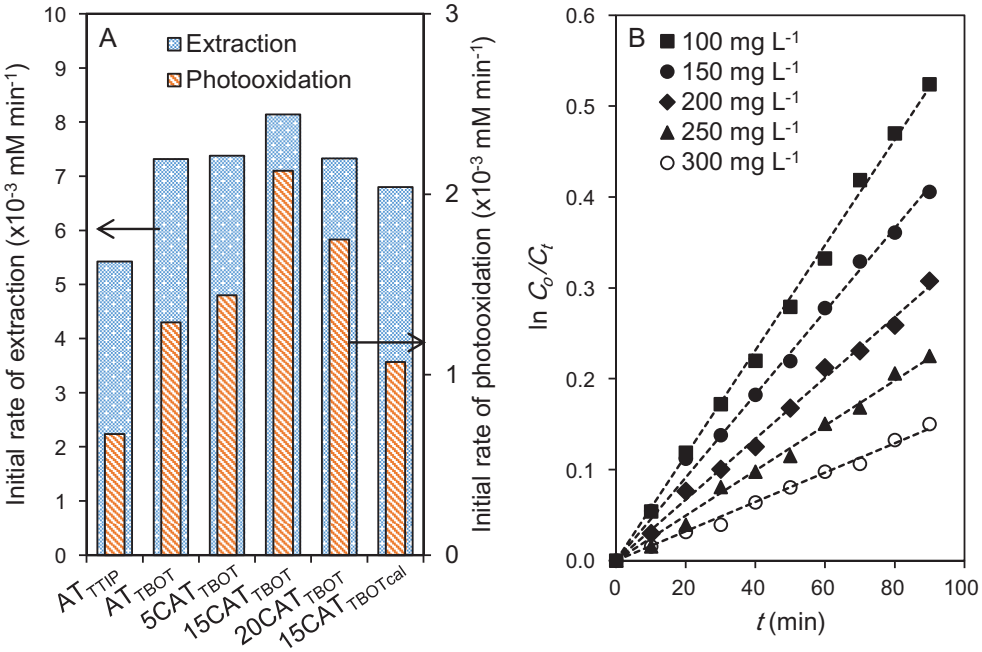

Fig. 9. (A) Performance of the catalysts on desulfurization of DBT (B) Photooxidation kinetics of DBT using 15 CAT_{TBOT} catalyst at different initial concentrations [catalyst dosage is 0.8 g L^{-1}].

Table 2
Photooxidation of DBT at different initial concentration and pseudo-first-order apparent constant values by 15 CAT_{TBOT} [catalyst dosage 0.8 g L^{-1}].

Initial conc. C_o (mg L^{-1})	Rate, k_{app} ($\times 10^{-3}$ min^{-1})	Initial rate, r_o ($\times 10^{-1}$ mg L^{-1} min^{-1})
100	5.8	3.92
150	4.6	4.36
200	3.3	4.47
250	2.5	4.24
300	1.6	2.79

desulphurization of DBT, four important scavenging agents were used: potassium peroxodisulphate (PP), triethanolamine (TEOA), sodium hydrogen carbonate (SHC) and isopropanol (IP) as scavengers for electrons (e^-), holes (h^+), surface hydroxyl groups ($^{\cdot}OH_{ads}$) and hydroxyl groups in the bulk solution ($^{\cdot}OH_{bulk}$), respectively. From Fig. 10A, it can be seen that h^+ played a main role in photooxidation, assisted by $^{\cdot}OH_{ads}$, e^- and $^{\cdot}OH_{bulk}$. Consequently, it is proposed that, the electrons were excited from the valence band (VB) of TiO_2 to the existing impurity level (C 1s) under visible light irradiation (Fig. 10B), before migrating to the conduction band (CB), leaving h^+ at VB and impurity level [21,56]. h^+ could directly oxidize DBT, or produce $^{\cdot}OH_{ads}$ when reacted with H_2O or adsorbed OH^- groups on the surface of TiO_2 and oxidize DBT. In parallel, the excited e^- reduced oxygen to superoxide anion radicals ($\cdot O_2^-$), that is capable to oxidize DBT to $DBTO_2$ or react with H^+ to form $^{\cdot}OH_{bulk}$. A similar phenomenon was reported previously for the photodegradation of 2-chlorophenol using IS-FeOOH/MSN [57].

The detailed photooxidation path of DBT is proposed as in Fig. 11, which was confirmed using GC-MSD (Figs. S4–S6), and in line with the other previous works. As shown in the figure, the DBT (1) was first oxidized to dibenzothiophene 5-oxide (DBTO) (2) and then to dibenzothiophene 5,5-dioxide ($DBTO_2$) (3) [42]. A highly reactive 1,5-biradical intermediate may be formed when $DBTO_2$ (3) was photo-excited by visible light irradiation, before being hydrogenated by OH groups of the catalyst and decomposed to biphenyl (4) [58]. At the same time, it is assumed that the sulphur species escaped as a gas from the solution. Further irradiated biphenyl may lead to the formation of biphenyl radical, which then reacted with O_2 and degraded to benzaldehyde (5), benzyl alcohol (6) and acetophenone (7) [59], while, benzoic acid (9) was produced from oxidation of the benzaldehyde [60]. At the same time, biphenyl radical may also being hydrolyzed to form hydroxybiphenyl (8) [59], that could fragmented into phenol compound (10), which finally hydrogenated into cyclohexen-1-one and 2-cyclohexen-1-ol [61].

3.4. Application on other S-containing compounds

The potential of 15 CAT_{TBOT} catalyst was also examined on photocatalytic oxidative desulphurization of other S-containing compounds; thiophene (T), benzothiophene (BT) and 4,6-dimethyldibenzothiophene (4,6-DMDBT), and their performance rates were compared with DBT. As can be observed in Fig. 12, the photocatalytic performance decreased in the following order: 4,6-DMDBT > DBT > BT > T. This is most probably due to their difference in electron densities which are 5.760, 5.758, 5.739 and 5.696, respectively [62]. It has been reported previously that the higher electron density of a sulphur atom has led to a higher reaction rate of a sulphur-containing compound [63]. This might generally explained a slightly higher performance rate of the catalyst towards 4,6-DMDBT molecule than DBT [64].

4. Conclusion

In conclusion, amorphous TiO_2 was successfully synthesized using different titanium precursors by the sol-gel method, and was self-doped with carbon by the electrochemical technique with different electrolysis time. This was then used as a catalyst in the photooxidative desulphurization of DBT under visible light irradiation. The physicochemical properties of the catalysts were examined by XRD, N_2 physisorption, FTIR, TEM, EDX, XPS, ESR and UV–Vis DRS. XRD analysis identified the amorphous phase of the catalysts which are not affected by the presence of dopants. The N_2 physisorption analysis verified the presence of larger bimodal pore structures in the range of 20–100 nm for AT_{TBOT}, as compared to AT_{TTIP} with bimodal pore structures in the range of 3–50 nm. The existence of larger pores was beneficial for greater absorptivity of DBT molecules, which consequently enhanced photocatalytic activity. FTIR and XPS analyses revealed that the use of longer chain TBOT to synthesize AT_{TBOT} and electrolysis process in the presence of weak base TEAP led to the introduction of C to form O–Ti–C and Ti–O–C bonds into the AT_{TBOT} network. The highest performance of 15 CAT_{TBOT} was promoted by the presence of a narrow band gap, good

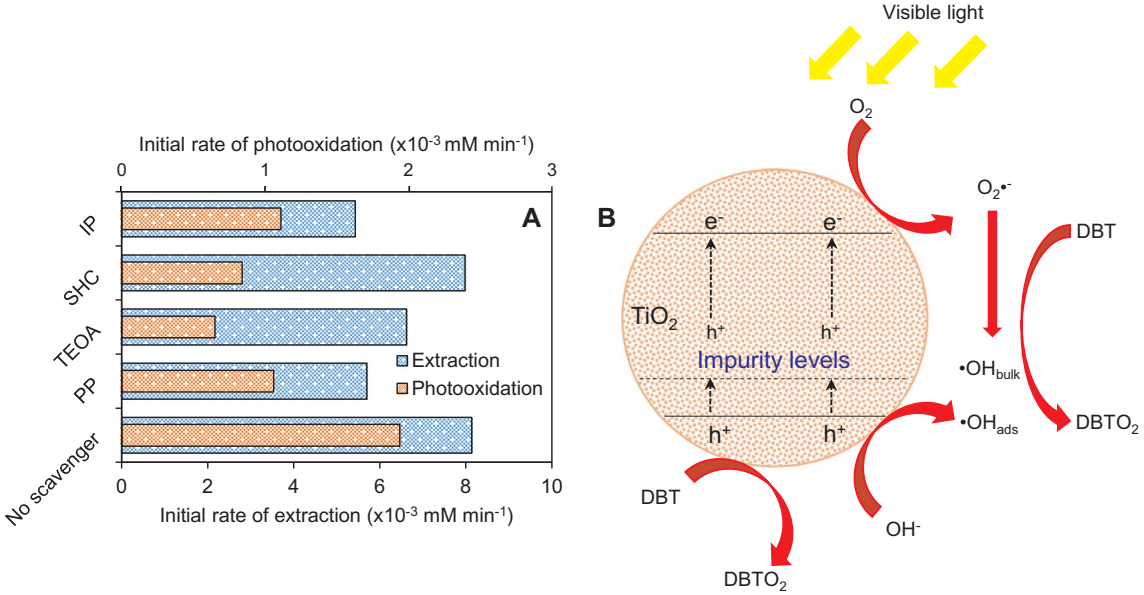

Fig. 10. (A) Sulfur removal efficiencies of DBT in the presence of electron scavenger, hole scavenger, $\cdot OH_{ads}$ and $\cdot OH_{bulk}$ scavenger by 15 CAT_{TBOT} (B) Schematic illustration of DBT removal under visible light irradiation [catalyst dosage 0.8 g L^{-1}, initial concentration is 100 mg L^{-1}].

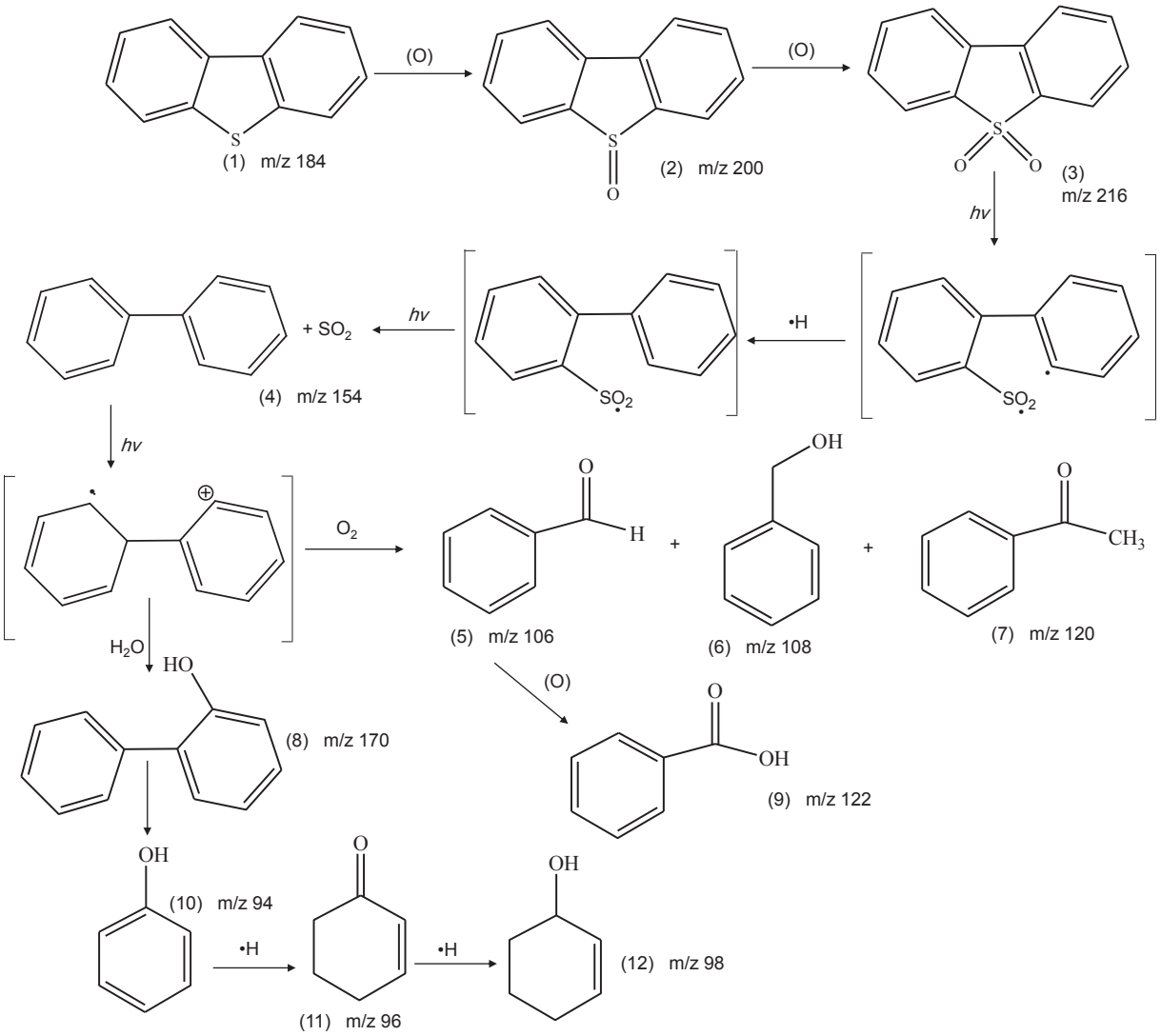

Fig. 11. Possible DBT photooxidation path.

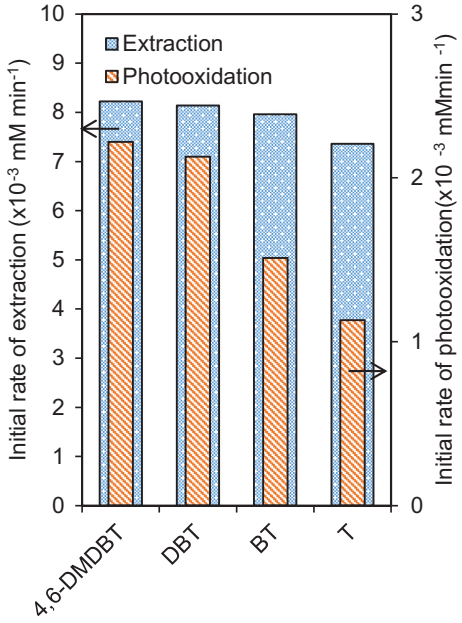

Fig. 12. Application of 15 CAT_{TBOT} on removal of different S-containing compounds.

interactions between C with AT_{TBOT} support, as well as its physical properties, which enhanced photoactivity under visible light. The higher numbers of Ti–O–C and O–Ti–C, bonds, as well as an appropriate surface area and pore volume, increased the number of active sites and offered good surface contact with light for transporting and/or capturing electrons for enhancement of photocatalytic activity. The kinetic studies revealed that the photocatalytic oxidative desulphurization of DBT using 15 CAT_{TBOT} followed a pseudo-first order Langmuir-Hinshelwood model where the adsorption was the controlling step. Therefore, the synthesized catalyst could be a promising candidate for its practical applications in environmental purification and may also aid in the improvement of visible-light-oriented catalysts for photodegradation of various pollutants specifically in the sulphur removal.

Acknowledgments

The authors are grateful for the financial support by the Research University Grant from Universiti Teknologi Malaysia (Grant No. 12H70 and 4F423) and the awards of MyPhD Scholarship (Che Ku Nor Liana Che Ku Hitam) from Ministry of Higher Education, Malaysia.

Appendix A. Supplementary data

Supplementary data associated with this article can be found, in the

online version, at http://dx.doi.org/10.1016/j.fuel.2017.12.035.

References

[1] Lin F, Jiang Z, Tang N, Zhang C, Chen Z, Liu T, et al. Photocatalytic oxidation of thiophene on RuO_2/SO_4^{2-}-TiO_2: insights for cocatalyst and solid-acid. Appl Catal B-Environ 2016;188:253–8.
[2] Wang L, Cai H, Li S, Mominou N. Ultra-deep removal of thiophene compounds in diesel oil over catalyst TiO_2/Ni-ZSM-5 assisted by ultraviolet irradiating. Fuel 2013;105:752–6.
[3] Tao H, Nakazato T, Sato S. Energy-efficient ultra-deep desulfurization of kerosene based on selective photooxidation and adsorption. Fuel 2009;88:1961–9.
[4] Lei W, Shuzhen L, Haijun C, Yanyan X, Xihui W, Yujing C. Ultra-deep desulfurization of fuel with metal complex of Chitosan Schiff Base assisted by ultraviolet. Fuel 2012;94:165–9.
[5] Jusoh NWC, Jalil AA, Triwahyono S, Karim AH, Salleh NF, Annuar NHR, et al. Structural rearrangement of mesostructured silica nanoparticles incorporated with ZnO catalyst and its photoactivity: effect of alkaline aqueous electrolyte concentration. Appl Surf Sci 2015;330:10–9.
[6] Pérez-Larios A, Lopez R, Hernández-Gordillo A, Tzompantzi F, Gómez R, Torres-Guerra LM. Improved hydrogen production from water splitting using TiO2–ZnO mixed oxides photocatalysts. Fuel 2012;100:139–43.
[7] Wang X, Wang Q, Li F, Yang W, Zhao Y, Hao Y, et al. Novel BiOCl–C3N4 heterojunction photocatalysts: in situ preparation via an ionic-liquid-assisted solvent-thermal route and their visible-light photocatalytic activities. Chem Eng J 2013;234:361–71.
[8] Krylova G, Na C. Photoinduced crystallization and activation of amorphous titanium dioxide. J Phys Chem C 2015;119:12400–7.
[9] Lee S, Lee K, Kim WD, Lee S, Shin DJ, Lee DC. Thin amorphous TiO_2 shell on CdSe nanocrystal quantum dots enhances photocatalysis of hydrogen evolution from water. J Phys Chem C 2014;118:23627–34.
[10] Randorn C, Irvine JTS, Robertson P. Synthesis of visible-light-activated yellow amorphous TiO_2 photocatalyst. Int J Photoenergy 2008:426872–7.
[11] Kim Y, Hwang HM, Wang L, Kim I, Yoon Y, Lee H. Solar-light photocatalytic disinfection using crystalline/amorphous low energy band gap reduced TiO2. Sci Rep 2016;6:25203–12.
[12] Zhu W, Xu Y, Li H, Dai B, Xu H, Wang C, et al. Photocatalytic oxidative desulfurization of dibenzothiophene catalyzed by amorphous TiO2 in ionic liquid. Korean J Chem Eng 2014;31(2):211–7.
[13] De Witte K, Busuioc AM, Meynen V, Mertens M, Bilba N, Van Tendeloo G, et al. Influence of the synthesis parameters of TiO2–SBA-15 materials on the adsorption and photodegradation of rhodamine-6G. Micropor Mesopor Mater 2008;110:100–10.
[14] Simonsen ME, Søgaard EG. Sol–gel reactions of titanium alkoxides and water: influence of pH and alkoxy group on cluster formation and properties of the resulting products. J Sol-Gel Sci Technol 2010;53:485–97.
[15] Etacheri V, Michlits G, Seery MK, Hinder SJ, Pillai SC. A highly efficient TiO2-XCx nano-heterojunction photocatalyst for visible light induced antibacterial applications. ACS Appl Mater Interfaces 2013;5(5):1663–72.
[16] Jiang L, Huang Y, Liu T. Enhanced visible-light photocatalytic performance of electrospun carbon-doped TiO2/halloysite nanotube hybrid nanofibers. J Colloid Interface Sci 2015;439:62–8.
[17] Zhang L, Jing D, She X, Liu H, Yang D, Lu Y, et al. Heterojunctions in g-C3N4/TiO2(B) nanofibres with exposed (001) plane and enhanced visible-light photoactivity. J Mater Chem A 2014;2:2071–8.
[18] Zaid HFM, Chong FK, Mutalib MIA. Photooxidative–extractive deep desulfurization of diesel using Cu–Fe/TiO2 and eutectic ionic liquid. Fuel 2015;156:54–62.
[19] Jusoh R, Jalil AA, Triwahyono S, Kamarudin NHN. Synthesis of dual type Fe species supported mesostructured silica nanoparticles: synergistical effects in photocatalytic activity. RSC Adv 2015;5:9727–36.
[20] Sidik SM, Jalil AA, Triwahyono S, Abdullah TAT, Ripin A. CO2 reforming of CH4 over Ni/mesostructured silica nanoparticles (Ni/MSN). RSC Adv 2015;5:37405–14.
[21] Jaafar NF, Jalil AA, Triwahyono S. Visible-light photoactivity of plasmonic silver supported on mesoporous TiO2 nanoparticles (Ag-MTN) for enhanced degradation of 2-chlorophenol: limitation of Ag-Ti interaction. Appl Surf Sci 2017;392:1068–77.
[22] Khusnun NF, Jalil AA, Triwahyono S, Jusoh NWC, Johari A, Kidam K. Interaction between copper and carbon nanotubes triggers their mutual role in the enhanced photodegradation of p-chloroaniline. PCCP 2016;18:12323–31.
[23] Sidik SM, Triwahyono S, Jalil AA, Aziz MAA, Fatah NAA, Teh LP. Tailoring the properties of electrolyzed Ni/mesostructured silica nanoparticles (MSN) via different Ni-loading methods for CO2 reforming of CH4. J CO2 Util 2016;13:71–80.
[24] Jalil AA, Kurono N, Tokuda M. Facile synthesis of ethyl 2-arylpropenoates by cross-coupling reaction using electrogenerated highly reactive zinc. Tetrahedron 2002;58:7477–84.
[25] Hitam CNC, Jalil AA, Triwahyono S, Ahmad A, Jaafar NF, Salamun N, et al. Synergistic interactions of Cu and N on surface altered amorphous TiO2 nanoparticles for enhanced photocatalytic oxidative desulfurization of dibenzothiophene. RSC Adv 2016;6:76259–68.
[26] Jalil AA, Kurono N, Tokuda M. Facile synthesis of 2-arylpropenoic acid esters by cross-coupling using electrogenerated highly reactive zinc and a palladium catalyst. Synlett 2001;12:1944–6.
[27] Jalil AA, Kurono N, Tokuda M. Synthesis of the precursor of anti-inflammatory agents by cross-coupling using electrogenerated highly reactive zinc. Synthesis 2002;18:2681–6.
[28] Li Z, Zhu Y, Wang J, Guo Q, Li J. Size-controlled synthesis of dispersed equiaxed amorphous TiO2 nanoparticles. Ceram Int 2015;41:9057–62.
[29] Sinkó K. Influence of chemical conditions on the nanoporous structure of silicate aerogels. Materials 2010;3:704–40.
[30] Najafian A, Rahimi R, Zargari S, Mahjoub-Moghaddas M, Nazemi A. Synthesis and photocatalytic activity of V-doped mesoporous TiO2 photosensitized with porphyrin supported by SBA-15. Res Chem Intermed 2016;42:3441–58.
[31] Triantafyllidis KS, Deliyanni EA. Desulfurization of diesel fuels: adsorption of 4,6-DMDBT on different origin and surface chemistry nanoporous activated carbons. Chem Eng J 2014;236:406–14.
[32] Miyamoto J, Kanoh H, Kaneko K. Pore structures and adsorption characteristics of activated carbon fibers having both micro- and mesopores. Prepr Pap Am Chem Soc Div Fuel Chem 2005;50(1):2–3.
[33] Wang Q, Chen M, Zhu N, Shi X, Jin H, Zhang Y, et al. Preparation of AgI sensitized amorphous TiO2 as novel high-performance photocatalyst for environmental applications. J Colloid Interface Sci 2015;448:407–16.
[34] Karim AH, Jalil AA, Triwahyono S, Sidik SM, Kamarudin NHN, Jusoh R, et al. J Colloid Interface Sci 2012;386:307–14.
[35] Fatah NAA, Triwahyono S, Jalil AA, Ahmad A, Abdullah TAT. Appl Catal A-Gen 2016;516:135–43.
[36] Jesurani S, Kanagesan S, Velmurugan R, Thirupathi C, Sivakumar M, Kalaivani T. Mater Lett 2011;65:3305–8.
[37] Wen Y, Ding H, Shan Y. Preparation and visible light photocatalytic activity of Ag/TiO2/graphene nanocomposite. Nanoscale 2011;3:4411–7.
[38] Lin W, Frei H. Bimetallic redox sites for photochemical CO2 splitting in mesoporous silicate sieve. C R Chim 2006;9:207–13.
[39] Kucharzyk KH, Crawford RL, Cosens B, Hess TF. Development of drinking water standards for perchlorate in the United States. J Environ Manage 2009;91:303–10.
[40] Lin H, Long J, Gu Q, Zhang W, Ruan R, Li Z, et al. In situ IR study of surface hydroxyl species of dehydrated TiO2: towards understanding pivotal surface processes of TiO2 photocatalytic oxidation of toluene. PCCP 2012;14:9468–74.
[41] Belskaya OB, Duplyakin VK, Likholobov VA. Molecular design of precursor in the synthesis of catalytic nanocomposite system Pt-Al2O3. Smart Nanocompos 2011;1:99–200.
[42] Zarrabi M, Entezari MH, Goharshadi EK. Photocatalytic oxidative desulfurization of dibenzothiophene by C/TiO2@MCM-41 nanoparticles under visible light and mild conditions. RSC Adv 2015;5:34652–62.
[43] Park Y, Kim W, Park H, Tachikawa T, Majima T, Choi W. Carbon-doped TiO2 photocatalyst synthesized without using an external carbon precursor and the visible light activity. Appl Catal B-Environ 2009;91:355–61.
[44] Lin C, Song Y, Cao L, Chen S. Effective photocatalysis of functional nanocomposites based on carbon and TiO2 nanoparticles. Nanoscale 2013;5:4986–92.
[45] Liu G, Han C, Pelaez M, Zhu D, Liao S, Likodimos V, et al. Synthesis, characterization and photocatalytic evaluation of visible light activated C-doped TiO2 nanoparticles. Nanotechnology 2012;23:293993–4003.
[46] Konstantinova EA, Kokorin AI, Lips K, Sakhtivel S, Kisch H. EPR study of the illumination effect on properties paramagnetic centers in nitrogen-doped TiO2 active in visible light photocatalysis. Appl Magn Reson 2009;35:421–7.
[47] Chen X, Mao SS. Titanium dioxide nanomaterials: synthesis, properties, modifications, and applications. Chem Rev 2007;107:2891–959.
[48] Valentin CD, Pacchioni G. Trends in non-metal doping of anatase TiO2: B, C, N and F. Catal Today 2013;206:12–8.
[49] Mahshid S, Askari M, Ghamsari MS. Synthesis of TiO2 nanoparticles by hydrolysis and peptization of titanium isopropoxide solution. J Mater Process Technol 2007;189:296–300.
[50] Salleh NFM, Jalil AA, Triwahyono S, Efendi J, Mukti RR, Hameed BH. New insight into electrochemical-induced synthesis of NiAl2O4/Al2O3: synergistic effect of surface hydroxyl groups and magnetism for enhanced adsorptivity of Pd(II). Appl Surf Sci 2015;349:485–95.
[51] Zheng S, Gao L, Zhang Q, Guo J. Synthesis, characterization and photocatalytic properties of titania-modified mesoporous silicate MCM-41. J Mater Chem 2000;10:723–7.
[52] Jusoh NWC, Jalil AA, Triwahyono S, Setiabudi HD, Sapawe N, Satar MAH, et al. Sequential desilication–isomorphous substitution route to prepare mesostructured silica nanoparticles loaded with ZnO and their photocatalytic activity. Appl Catal A-Gen 2013;468:276–87.
[53] Jaafar NF, Jalil AA, Triwahyono S, Efendi J, Mukti RR, Jusoh R, et al. Direct in situ activation of Ag0 nanoparticles in synthesis of Ag/TiO2 and its photoactivity. Appl Surf Sci 2015;338:75–84.
[54] Jaafar NF, Jalil AA, Triwahyono S, Shamsuddin N. New insights into self-modification of mesoporous titania nanoparticles for enhanced photoactivity: effect of microwave power density on formation of oxygen vacancies and Ti3+ defects. RSC Adv 2015;5:90991–1000.
[55] Idris A, Hassan N, Rashid R, Ngomsik A. Kinetic and regeneration studies of photocatalytic magnetic separable beads for chromium (VI) reduction under sunlight. J Hazard Mater 2011;186:629–35.
[56] Zarrabi M, Entezari MH. Modification of C/TiO2@MCM-41 with nickel nanoparticles for photocatalytic desulfurization enhancement of a diesel fuel model under visible light. J Colloid Interface Sci 2015;457:353–9.
[57] Jusoh R, Jalil AA, Triwahyono S, Idris A, Noordin MY. Photodegradation of 2-chlorophenol over colloidal α-FeOOH supported mesostructured silica nanoparticles: influence of a pore expander and reaction optimization. Sep Purif Technol 2015;149:55–64.
[58] Shiraishi Y, Tachibana K, Hirai T, Komasawa I. Photochemical production of biphenyls from oxidized sulfur compounds obtained by oxidative desulfurization of light oils. Energy Fuel 2003;17:95–100.
[59] Silva JPD, Ferreira LFV. A comparative study of the photochemistry of biphenyl

adsorbed on cellulose and silicalite. Int J Photoenergy 2004;6(4):193–8.
[60] Amadelli R, Samiolo L, Maldotti A. Selective photooxidation and photoreduction processes at TiO2 surface-modified by grafted vanadyl. Int J Photoenergy 2011:259453–63.
[61] Liu X, Friend CM. Selective oxidation of cyclohexanol and 2-cyclohexen-1-ol on O/Au(111): the effect of molecular structure. Langmuir 2010;26(21):16552–7.
[62] Otsuki S, Nonaka T, Takashima N, Qian W, Ishihara A, Imai T, et al. Oxidative desulfurization of light gas oil and vacuum gas oil by oxidation and solvent extraction. Energy Fuel 2000;14:1232–9.
[63] Lu H, Zhang Y, Jiang Z, Li C. Aerobic oxidative desulfurization of benzothiophene, dibenzothiophene and 4,6-dimethyldibenzothiophene using an Anderson-type catalyst [(C18H37)2N(CH3)2]5[IMo6O24]. Green Chem 2010;12:1954–8.
[64] Matsuzawa S, Tanaka J, Sato S, Ibusuki T. Photocatalytic oxidation of dibenzothiophenes in acetonitrile using TiO2: effect of hydrogen peroxide and ultrasound irradiation. J Photochem Photobiol A 2002;149:183–9.